Going in circles: Slender body analysis of a self-propelling bent rod

Arkava Ganguly and Ankur Gupta*
Department of Chemical and Biological Engineering, University of Colorado, Boulder, Colorado 80309, USA

(Received 19 October 2022; accepted 6 January 2023; published 20 January 2023)

We study the two-dimensional motion of a self-propelling asymmetric bent rod. By employing slender body theory and the Lorentz reciprocal theorem, we determine particle trajectories for different geometric configurations and arbitrary surface activities. Our analysis reveals that all particle trajectories can be mathematically expressed through the equation for a circle. The rotational speed of the particle dictates the frequency of the circular motion and the ratio of translational and rotational speeds describes the radius of the circular trajectory. We find that even for uniform surface activity, geometric asymmetry is sufficient to induce a self-propelling motion. Specifically, for uniform surface activity, we observe (i) when bent rod arm lengths are equal, the particle only translates, (ii) when the length of one arm is approximately four times the length of the other arm and the angle between the arms is approximately $\frac{\pi}{2}$, the rotational and translational speeds are at their maximum. We explain these trends by comparing the impact of geometry on the hydrodynamic resistance tensor and the active driving force. Overall, the results presented here quantify self-propulsion in composite-slender bodies and motivate future research into self-propulsion of highly asymmetric particles.

DOI: 10.1103/PhysRevFluids.8.014103

I. INTRODUCTION

Biological entities typically propel by the beating of cellular appendages like flagella or cilia in asymmetric, wavelike patterns [1–6]. To mimic biological motion, synthetic propellers have garnered attention due to their promising applications in medicine [7–10], microfluidic devices [11,12], environmental remediation [13,14], and the fabrication of self-repairing surfaces [15,16]. Broadly speaking, there are two categories of propulsion mechanisms in synthetic particles. The first category of motion is externally actuated, where the propulsion is driven through an external field. Instances of externally driven propulsion include magnetophoresis due to a magnetic field [17–20], acoustic propulsion through ultrasound [21–29], electrophoresis driven by constant electric fields [30–35], induced-charged electrophoresis due to AC electric fields [36–43], diffusiophoresis due to concentration gradients of solute(s) [44–49], and thermophoresis [50–52] because of temperature gradients. The second category of propulsion in synthetic particles is self-actuated, where the fields are generated by the particles themselves. Typical examples include self-diffusiophoresis and self-thermophoresis, among others [53–63]. The focus of this work is self-diffusiophoresis, though the results outlined here are readily extended to self-thermophoresis as well.

The most common example of self-diffusiophoresis reported in literature consists of a Janus sphere, where the motion is induced through an asymmetric reaction [60,64–68]. However, several studies have argued that asymmetry in reaction is not a necessary requirement for self-diffusiophoresis. Instead, geometric asymmetries also induce a self-diffusiophoretic motion,

*ankur.gupta@colorado.edu

even for a uniform surface activity. Existing theoretical analyses have largely focused on specific particle geometries such as spheroidal [69–73] and cylindrical [74,75]. However, the work by Shklyaev *et al.* [76] and Daddi-Moussa-Ider *et al.* [77] demonstrates that a perturbation to these shapes can modify the direction and speed of the propulsion. Clearly, geometry plays a key role in self-diffusiophoretic propulsion.

To go beyond these typical shapes, recent literature utilized slender body theory (SBT) [78–80] to predict the motion of self-diffusiophoretic particles. Schnitzer and Yariv [75], and Yariv [81] studied the motion of a straight slender rod with an arbitrary cross-section, arbitrary surface activity, and first-order reaction kinetics. Poehnl and Uspal [82] investigated catalytic helical particles to obtain a good agreement between their SBT prediction and boundary element calculations. Katsamba *et al.* [83,84] outlined a comprehensive SBT framework that can predict the motion for arbitrary surface activity and an arbitrary three-dimensional axisymmetric geometry.

While the studies described above advance our understanding of self-propulsion in slender bodies, they focus on a slender body with a single axis. In this work, we analyze the self-diffusiophoretic motion of a composite slender body, i.e., a bent-rod geometry. Our motivation to study a bent-rod is twofold. First, such an asymmetric geometry has been experimentally studied by Kümmel *et al.* [85], who reported a circular motion in L-shaped particles, which was later extended by Rao *et al.* [86] who studied slender rods bent at different angles. Here, we describe the motion of similar geometries through SBT and do not invoke an external force and torque [87]. Second, the hydrodynamics of a passive bent-rod have been studied in detail by Roggeveen and Stone [88]. The authors calculate hydrodynamic mobility for such a geometry, which we utilize to predict the motion of a self-propelling bent rod. In Sec. II, we calculate the excess solute concentration and obtain the slip velocity at the particle surface. Next, we evaluate the particle motion by using the Lorentz reciprocal theorem [82,89,90]. Subsequently, we find that the particle trajectory is always circular. In Sec. III, we validate our predictions with the experimental results of Kümmel *et al.* [85] and obtain good agreement without any fitting parameters. Next, we investigate the scenario of uniform surface flux. Our model reveals the impact of geometry on the circular motion of particles. For specific geometric parameters, the particle rotation arising out of the translation-rotation coupling and surface activity individually go to zero, causing the particles to move in a straight line. We show that the translation and rotation speeds are maximum when one arm is approximately four times longer than the other and the arms are at right angles to each other. In Sec. IV, we summarize our results, discuss the implications of our findings, and outline future directions.

II. THEORETICAL FRAMEWORK

A. Particle geometry

We follow the geometric description of a bent-rod outlined in Roggeveen and Stone [88]. The bent-rod is composed of two cylindrical arms aligned at an angle θ; see Fig. 1. The lengths of the two arms are assumed to be $(\frac{1}{2}+q)\ell$ and $(\frac{1}{2}-q)\ell$, where ℓ is the total length and q is the length asymmetry parameter. We note that $q \in [-\frac{1}{2}, \frac{1}{2}]$. Both the arms are assumed to be of the same radius a such that $\frac{a}{\ell} = \epsilon \ll 1$. The rod self-propels due to diffusiophoresis, induced by a surface reaction. We note that though the analysis presented here focuses on a diffusiophoretic process [75,81,91], the results are also readily extendable to thermophoretic propulsion [52,85].

We nondimensionalize the coordinate system by ℓ. We introduce the arc-length parameter s to describe the position along the centerline of the rod such that $-\frac{1}{2}+q \leqslant s \leqslant \frac{1}{2}+q$. $s=0$ represents the hinge, whereas $s = q \pm \frac{1}{2}$ denote the end of the two arms. For consistency, we refer to the arm where $0 \leqslant s \leqslant q+\frac{1}{2}$ as the positive arm and the arm where $-\frac{1}{2}+q \leqslant s < 0$ as the negative arm. The shape of the bent rod is thus dictated by q and θ.

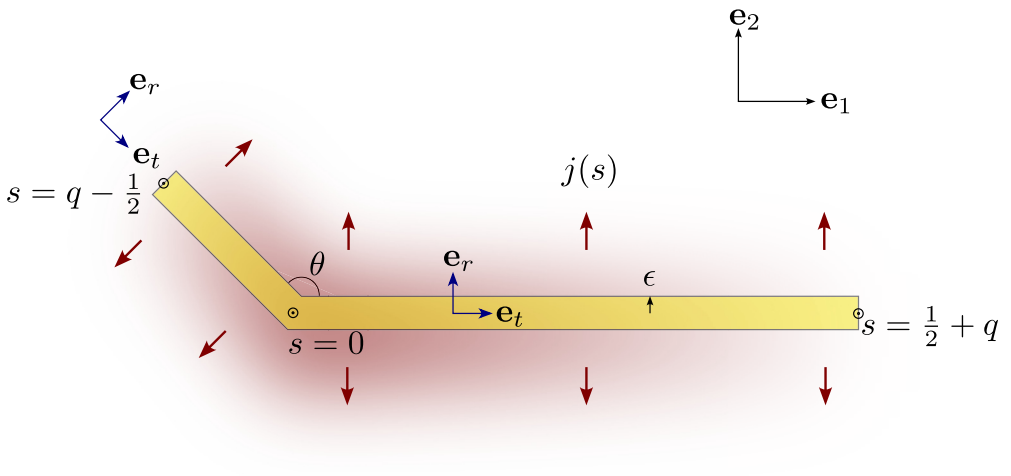

FIG. 1. Nondimensional schematic of the problem setup. We consider a rigid bent rod composed of two cylindrical arms of equal radius a, aligned at an angle θ. The length of the two arms are $(\frac{1}{2}+q)\ell$ and $(\frac{1}{2}-q)\ell$. Therefore, the total length of the bent rod is ℓ. We focus on the slender limit, i.e., $\epsilon = \frac{a}{\ell} \ll 1$. The rod self-propels due to solute flux on the rod in the $\mathbf{e}_1$-$\mathbf{e}_2$ plane and can rotate about the $\mathbf{e}_1 \times \mathbf{e}_2$ plane. $\mathbf{e}_r$-$\mathbf{e}_t$ represent the directions normal and tangential to the bent rod. To nondimensionalize our problem setup, we scale all the lengths by ℓ. s represents the dimensionless coordinate along the rod. $s = 0$ is the hinge and $s = \frac{1}{2} \pm q$ are the ends of two arms. The dimensionless solute flux is represented by $j(s)$. Both $\mathbf{e}_1$-$\mathbf{e}_2$ and $\mathbf{e}_r$-$\mathbf{e}_t$ are defined in the reference frame of the particle. $\mathbf{e}_1$ is defined such that it is aligned with the positive arm, i.e., $0 \leqslant s \leqslant \frac{1}{2} + q$. $\mathbf{e}_2$ is perpendicular to $\mathbf{e}_1$. $\mathbf{e}_r$ and $\mathbf{e}_t$ are expressed as a function of $\mathbf{e}_1$ and $\mathbf{e}_2$; see Eq. (1). The laboratory reference frame is given by $\mathbf{e}_x$-$\mathbf{e}_y$; see Sec. II D.

We assume that the rod only propels in the $\mathbf{e}_1$-$\mathbf{e}_2$ plane and can rotate about the $\mathbf{e}_3 = \mathbf{e}_1 \times \mathbf{e}_2$ axis. The direction $\mathbf{e}_1$ is always assumed to be aligned with the positive arm. For convenience, we also define $\mathbf{e}_t$ and $\mathbf{e}_r$ as the tangential and normal directions to the rod, respectively, such that

$$\mathbf{e}_t = \begin{cases} -\cos\theta\, \mathbf{e}_1 - \sin\theta\, \mathbf{e}_2 & s < 0 \\ \mathbf{e}_1 & s \geqslant 0 \end{cases}, \tag{1a}$$

$$\mathbf{e}_r = \begin{cases} -\sin\theta\, \mathbf{e}_1 + \cos\theta\, \mathbf{e}_2 & s < 0 \\ \mathbf{e}_2 & s \geqslant 0 \end{cases}. \tag{1b}$$

Note that both $\mathbf{e}_1$-$\mathbf{e}_2$ and $\mathbf{e}_t$-$\mathbf{e_r}$ are in the particle frame of reference and moves with the particle. In Sec. II D, we define $\mathbf{e}_x$-$\mathbf{e}_y$ as our universal frame of reference to obtain equations for the particle trajectories; see Eq. (16). The position of a point on the particle centerline is $\mathbf{x}_h(s) = s\mathbf{e}_t$. The center of mass of the bent-rod is denoted as $\mathbf{x}_{\text{com}}$. To model self-propulsion through catalytic activity, we follow the common practice in literature [58,75,81,82,92–94], and we assume a solute flux $j(s)$ on the particle surface (the mathematical definition of $j(s)$ is provided later). The induced translation and rotation velocities of the particle are denoted by $\mathbf{U}$ and $\mathbf{\Omega}$, respectively. The objective of this paper is to determine the particle trajectory in the limit $\epsilon \ll 1$ for a given q, θ, and $j(s)$. The limit $\epsilon \ll 1$ enables us to invoke first-order slender body theory to evaluate $\mathbf{U}$ and $\mathbf{\Omega}$. We follow the approach outlined in Schnitzer and Yariv [75] and Poehnl and Uspal [82] to obtain the excess solute concentration profile and effective slip velocity. Next, we employ the geometric resistance coefficients obtained from Roggeven and Stone [88] and use the Lorentz reciprocal theorem to obtain the particle trajectory for a self-propelling bent rod. Since we utilize first-order slender body theory, we superpose the concentration and hydrodynamic effects of the two arms and neglect the higher-order corrections; see Appendix A. We acknowledge that our analysis ignores

any circumferential variations in the solute flux and solute concentration arising out of these higher order corrections. These effects have been discussed in-depth by Katsamba *et al.* [83,84] and Poehnl and Uspal [82].

B. Concentration profile

We seek to evaluate the concentration of the solute at the particle surface for a given geometry and surface flux. To do so, we define dimensionless surface flux $j(s)$ scaled by reference flux J_{ref}. We define $c(s, r)$ to be dimensionless solute concentration, scaled by $\frac{aJ_{\text{ref}}}{D}$, where D is the solute diffusivity. Mathematically, our objective is to evaluate concentration at the slip plane $c_s(s)$ for a given q, θ and $j(s)$. We note that $c_s(s)$ is equivalent to the surface concentration from the outer solution $c^{\text{out}}(s, \epsilon)$ [75,82,95] (also see Appendix A). We define the Péclet number of the rod as $\text{Pe} = \frac{U_{\text{ref}}\ell}{D}$, where U_{ref} is a typical velocity scale. For representative values, we focus on Ref. [96]. Here, catalytic spheres with 2 μm diameters were driven in H_2O_2 solutions. $D = O(10^{-8})$ m^2/s, $\ell_{\text{ref}} = O(10^{-6})$ m, and $U_{\text{ref}} = O(10^{-5})$ m/s. Therefore, $\text{Pe} = O(10^{-3})$. This helps us justify neglecting convection and unsteady terms in Eq. (2) [additional justification is provided after Eq. (17)]. Therefore, we write

$$\nabla^2 c = 0, r \geqslant \epsilon. \tag{2}$$

The diffusiophoretic activity is represented with a surface flux boundary condition,

$$-\epsilon \hat{\mathbf{n}} \cdot \nabla c = j(s), \ r = \epsilon, \tag{3a}$$

where $\hat{\mathbf{n}}$ is the surface normal vector. The far field boundary condition for solute concentration reads

$$c = 0, r \to \infty. \tag{3b}$$

Since $\epsilon \ll 1$, we use boundary-layer theory [95] to evaluate $c_s(s)$. As outlined in Appendix A, we divide the fluid volume into an inner and an outer region in the radial direction $\mathbf{e}_r$. In the inner region, we stretch the coordinates such that $\rho = r\epsilon^{-1}$ and evaluate $c^{\text{in}}(s, \rho)$ with the boundary condition in Eq. (3a). Subsequently, in the outer region, we evaluate $c^{\text{out}}(s, r)$ as a line integral of diffusive sources of strength $\alpha(s)$. We determine $\alpha(s)$ via an asymptotic matching $c_{\text{in}}(s, \infty) = c_{\text{out}}(s, \epsilon)$. From the leading order behavior, we obtain $\alpha(s) = \frac{j(s)}{2}$, which gives

$$c_s(s) = \frac{1}{2}\int_{q-\frac{1}{2}}^{q+\frac{1}{2}} \frac{j(s')}{|\mathbf{x}_h(s) + \epsilon \mathbf{e}_r(s) - \mathbf{x}_h(s')|} ds'. \tag{4}$$

The expression for $c_s(s)$ in Eq. (4) is consistent with the results of Schnitzer and Yariv [75] and Poehnl and Uspal [82]. Our analysis deviates from previous studies since we account for a composite slender body where $\mathbf{e}_t$ and $\mathbf{e}_r$ are different for the two arms; see Appendix A for quantitative comparison with direct numerical simulations. We define the concentration differences between the junction and the respective end-points as $\Delta c_0^{q+\frac{1}{2}} = c_s(q + \frac{1}{2}) - c_s(0)$ and $\Delta c^0_{q-\frac{1}{2}} = c_s(0) - c_s(q - \frac{1}{2})$. As we show later, $\Delta c_0^{q+\frac{1}{2}}$ and $\Delta c^0_{q-\frac{1}{2}}$ drive particle motion.

C. Particle velocity

We define a dimensionless fluid velocity $\mathbf{u}$ around the particle, scaled by a reference velocity U_{ref}, where $U_{\text{ref}} = \frac{k_B T a J_{\text{ref}} \lambda^2}{\mu D \ell}$, where k_B is the Boltzmann constant, T is the absolute temperature, and λ is the interaction length scale. Typically, $\lambda_{\text{ref}} = O(1) - O(10)$ nm [92]. Following the analyses in literature [75,83,93], we represent the interaction between the solute and the particle through a diffusiophoretic slip velocity [92,97], such that

$$\mathbf{u}_{\text{slip}} = M(s)(\mathbf{I} - \mathbf{e}_r\mathbf{e}_r) \cdot \nabla c_s = M(s)\frac{dc_s}{ds}\mathbf{e}_t, \tag{5}$$

where $M(s)$ is a nondimensional lumped mobility parameter scaled by $\frac{k_B T \lambda^2}{\mu}$. For simplicity, we consider $M(s) = 1$. To justify $M(s) = 1$, we note $M = O(\frac{U_{\text{ref}}}{k_B T c_{\text{ref}} \lambda^2/(\mu \ell_{\text{ref}})})$. For $k_B = O(10^{-23})$ J/K, $T = 300$ K, $c_{\text{ref}} = O(10^{24})$ m^{-3}, $\lambda = O(10^{-9})$ m [92], $\mu = O(10^{-3})$ Pa s, $\ell_{\text{ref}} = O(10^{-6})$ m, we get $M = O(1)$. Before proceeding with hydrodynamic calculations, we highlight that while Eq. (4) is derived for a diffusiophoretic system, the results can also be extended to a thermophoretic system. Specifically, the surface concentration c_s can be replaced by the dimensionless surface temperature (appropriately scaled by subtracting far-field temperature), and the point sources of solute flux can be replaced by point sources of heat flux.

The fluid velocity at the particle surface for a phoretic particle with translational velocity $\mathbf{U}$ (scaled by U_{ref}) and rotational velocity $\mathbf{\Omega}$ (scaled by $\frac{U_{\text{ref}}}{\ell}$) is described as

$$\mathbf{u}(s, \epsilon) = \mathbf{U} + \mathbf{\Omega} \times (\mathbf{x}_h - \mathbf{x}_{\text{com}}) + \mathbf{u}_{\text{slip}}. \tag{6}$$

In addition, the fluid velocity vanishes in the far-field, $\mathbf{u}(s, r \to \infty) \to 0$. Instead of solving for the velocity field, we employ the Lorentz reciprocal theorem to estimate $\mathbf{U}$ and $\mathbf{\Omega}$ [58,89]. To this end, we relate the fluid velocity $\mathbf{u}$ to an auxiliary Stokes flow around the same particle geometry, with velocity $\mathbf{u}^j$ as follows [82]:

$$\int_S \mathbf{u} \cdot \boldsymbol{\sigma}^j \cdot \hat{\mathbf{n}} \, dS = \int_S \mathbf{u}^j \cdot \boldsymbol{\sigma} \cdot \hat{\mathbf{n}} \, dS, \tag{7}$$

where the surface stresses $\boldsymbol{\sigma}$ and $\boldsymbol{\sigma}^j$ are scaled by $\frac{4\pi\mu U_{\text{ref}}}{\ell}$. The auxiliary problem has a no-slip condition at the rigid particle boundary, or

$$\mathbf{u}^j(s, \epsilon) = \mathbf{U}^j + \mathbf{\Omega}^j \times (\mathbf{x}_h - \mathbf{x}_{\text{com}}). \tag{8}$$

The fluid velocity vanishes in the far-field, $\mathbf{u}^j(s, r \to \infty) = \mathbf{u}^{j,\infty} \to \mathbf{0}$. Since the particle is constrained to move in the $\mathbf{e}_1$-$\mathbf{e}_2$ plane, $\mathbf{U} = U_1\mathbf{e}_1 + U_2\mathbf{e}_2$ and $\mathbf{\Omega} = \Omega_3\mathbf{e}_3$, implying we need three different auxiliary problems to obtain $\mathbf{U}$ and $\mathbf{\Omega}$. We consider the auxiliary problems to be classified as $j \in \{1, 2, 3\}$ such that

$$\mathbf{U}^1 = V_0\mathbf{e}_1, \ \mathbf{\Omega}^1 = \mathbf{0}, \tag{9a}$$

$$\mathbf{U}^2 = V_0\mathbf{e}_2, \ \mathbf{\Omega}^2 = \mathbf{0}, \tag{9b}$$

$$\mathbf{U}^3 = \mathbf{0}, \ \mathbf{\Omega}^3 = \Omega_0\mathbf{e}_3. \tag{9c}$$

We substitute Eqs. (6) and (8) into Eq. (7) to obtain

$$\begin{aligned} &\mathbf{U} \cdot \int_S \boldsymbol{\sigma}^j \cdot \hat{\mathbf{n}} \, dS + \mathbf{\Omega} \cdot \int_S (\mathbf{x}_h(s) - \mathbf{x}_{\text{com}}) \times \boldsymbol{\sigma}^j \cdot \hat{\mathbf{n}} \, dS + \int_S \mathbf{u}_{\text{slip}} \cdot \boldsymbol{\sigma}^j \cdot \hat{\mathbf{n}} \, dS \\ &= \mathbf{U}^j \cdot \int_S \boldsymbol{\sigma} \cdot \hat{\mathbf{n}} \, dS + \mathbf{\Omega}^j \cdot \int_S (\mathbf{x}_h(s) - \mathbf{x}_{\text{com}}) \times \boldsymbol{\sigma} \cdot \hat{\mathbf{n}} \, dS. \end{aligned} \tag{10}$$

Since a self-propelling particle is force and torque free [58,82,89], the right-hand side of Eq. (10) vanishes. Further, we can represent the surface integral of the hydrodynamic stress $\boldsymbol{\sigma}^j$ in terms of the line integral of the hydrodynamic force density $\mathbf{f}^j$, $\boldsymbol{\sigma}^j \cdot \hat{\mathbf{n}} \, dS = \mathbf{f}^j \, ds$. In slender body theory [80,90], the force density $\mathbf{f}^j$ (scaled by $4\pi\mu U_{\text{ref}}$) is defined as

$$\mathbf{f}^j(s) = -\mathscr{A}\left(\mathbf{I} - \frac{1}{2}\mathbf{e}_t\mathbf{e}_t\right) \cdot (\mathbf{u}^j - \mathbf{u}^{j,\infty}), \tag{11}$$

where $\mathscr{A} = \frac{1}{\ln(1/\epsilon)}$. The first two integrals in Eq. (10) are the dimensional hydrodynamic force $\mathbf{F}^j$ and torque $\mathbf{T}^j$ on the particle in the auxiliary flow problem. We thus obtain

$$\mathbf{U} \cdot \mathbf{F}^j + \mathbf{\Omega} \cdot \mathbf{T}^j + \int_{q-\frac{1}{2}}^{q+\frac{1}{2}} \mathbf{u}_{\text{slip}} \cdot \mathbf{f}^j(s) \, ds = 0. \tag{12}$$

To evaluate $\mathbf{F}^j$ and $\mathbf{T}^j$ for given $\mathbf{U}^j$ and $\mathbf{\Omega}^j$, we invoke the results of Roggeveen and Stone [88]. The resistance coefficients, as provided in Roggeveen and Stone [88], $\mathbf{A}$, $\mathbf{B}$, and $\mathbf{C}$ (see Appendix B), allow us to write

$$\begin{bmatrix} F_1^j \\ F_2^j \\ T_3^j \end{bmatrix} = \begin{bmatrix} A_{11} & A_{12} & \tilde{B}_{13} \\ A_{12} & A_{22} & \tilde{B}_{23} \\ \tilde{B}_{13} & \tilde{B}_{23} & C_{33} \end{bmatrix} \begin{bmatrix} U_1^j \\ U_2^j \\ \Omega_3^j \end{bmatrix}. \tag{13}$$

Substituting Eqs. (9), (11), and (13) in Eq. (12), we obtain a system of linear equations to calculate phoretic motion of the particle

$$\begin{bmatrix} U_1 \\ U_2 \\ \Omega_3 \end{bmatrix} = \mathscr{A}\mathbf{R}^{-1} \begin{bmatrix} \displaystyle\int_{(q-\frac{1}{2})}^{(q+\frac{1}{2})} \mathbf{u}_{\text{slip}} \cdot \left(\mathbf{I} - \frac{1}{2}\mathbf{e}_t\mathbf{e}_t\right) \cdot \mathbf{e}_1 \, ds \\ \displaystyle\int_{(q-\frac{1}{2})}^{(q+\frac{1}{2})} \mathbf{u}_{\text{slip}} \cdot \left(\mathbf{I} - \frac{1}{2}\mathbf{e}_t\mathbf{e}_t\right) \cdot \mathbf{e}_2 \, ds \\ \displaystyle\int_{(q-\frac{1}{2})}^{(q+\frac{1}{2})} \mathbf{u}_{\text{slip}} \cdot \left(\mathbf{I} - \frac{1}{2}\mathbf{e}_t\mathbf{e}_t\right) \cdot \mathbf{e}_3 \times (\mathbf{x}_h(s) - \mathbf{x}_{\text{com}}) \, ds \end{bmatrix}, \tag{14}$$

where $\mathbf{R}$ is the scaled resistance matrix. Note that the velocities are zero if $\mathbf{u}_{\text{slip}} = 0$. Substituting the expression of $\mathbf{u}_{\text{slip}}$ from Eq. (5) in the above equation and integrating, we obtain

$$\begin{bmatrix} U_1 \\ U_2 \\ \Omega_3 \end{bmatrix} = \mathscr{A} \begin{bmatrix} a_{11} & a_{12} & \tilde{b}_{13} \\ a_{12} & a_{22} & \tilde{b}_{23} \\ \tilde{b}_{13} & \tilde{b}_{23} & c_{33} \end{bmatrix} \begin{bmatrix} \frac{1}{2}\Delta c_0^{q+\frac{1}{2}} - \frac{\cos\theta}{2}\Delta c^0_{q-\frac{1}{2}} \\ -\frac{\sin\theta}{2}\Delta c^0_{q-\frac{1}{2}} \\ \frac{1}{4}\left(q-\frac{1}{2}\right)^2 \sin\theta \Delta c_0^{q+\frac{1}{2}} + \frac{1}{4}\left(q+\frac{1}{2}\right)^2 \sin\theta \Delta c^0_{q-\frac{1}{2}} \end{bmatrix}. \tag{15}$$

The coefficients of the mobility, i.e., $\mathbf{a}$, $\mathbf{b}$, and $\mathbf{c}$, can be obtained by inverting the resistance matrix in Eq. (13) (see Appendix B). We underscore that Eq. (15) is valid for an arbitrary $j(s)$, which modifies the values of $\Delta c_0^{q+\frac{1}{2}}$ and $\Delta c^0_{q-\frac{1}{2}}$. Additionally, Eq. (15) demonstrates that $\mathbf{U}$ and $\mathbf{\Omega}$ are dictated by concentration differences between the end-points and the hinge, i.e., $\Delta c_0^{q+\frac{1}{2}}$ and $\Delta c^0_{q-\frac{1}{2}}$, and the details of the spatial variation of the concentration profile between the hinge and the endpoints do not influence the particle motion.

D. Particle trajectories

$\mathbf{U}$ and $\mathbf{\Omega}$ given by Eq. (15) are in the reference frame of the particle, i.e., $\mathbf{e}_1$-$\mathbf{e}_2$. To obtain an equation of motion for the center of mass of the particle, i.e., $[x(t), y(t)]$, in a universal frame of reference $\mathbf{e}_x$-$\mathbf{e}_y$, we employ the rotation matrix as

$$\frac{d}{dt}\begin{bmatrix} x(t) \\ y(t) \\ \phi(t) \end{bmatrix} = \begin{bmatrix} \cos\phi(t) & -\sin\phi(t) & 0 \\ \sin\phi(t) & \cos\phi(t) & 0 \\ 0 & 0 & 1 \end{bmatrix} \begin{bmatrix} U_1 \\ U_2 \\ \Omega_3 \end{bmatrix}, \tag{16}$$

where ϕ is the angle between $\mathbf{e}_1$ and $\mathbf{e}_x$, and t is dimensionless time (scaled by ℓ/U_{ref}). Without any loss of generality, we define $x(0) = y(0) = \phi(0) = 0$. By integrating Eq. (16) in time, we get

$$(x(t) - \mathscr{X})^2 + (y(t) - \mathscr{Y})^2 = \mathscr{R}^2, \tag{17}$$

where $\mathscr{X} = -\frac{U_2}{\Omega_3}$ and $\mathscr{Y} = \frac{U_1}{\Omega_3}$. Equation (17) demonstrates that the particle moves in a circular trajectory where the center of the trajectory depends on the particle velocities. The radius of curvature of the trajectory is given by $\mathscr{R} = \sqrt{\frac{U_1^2+U_2^2}{\Omega_3^2}}$. The turn frequency of the particle is simply $f = \frac{\Omega_3}{2\pi}$. We note that Eq. (17) implicitly assumes that diffusion is significantly faster than the particle motion for $\text{Pe} = O(10^{-3})$, as previously discussed in Sec. II B. At this point, we will further

justify the pseudo-steady state assumption. Since our predictions suggest a circular trajectory, one might argue that the continuous release of solute could leave a trace behind that can build up over time. To quantify this effect, we briefly restore dimensions and perform an order of magnitude analysis. The total amount of solute released by the particle for time τ is given by $m \sim J(2\pi a\ell)\tau$, where J is the dimensional surface flux. The trace concentration C_{trace} can be estimated as $C_{\text{trace}} \sim m/(\frac{\pi}{6}\delta^3)$, where $\delta \sim \sqrt{4D\tau}$ is the diffusive boundary layer thickness. Upon rearrangement, it is easy to obtain that $\frac{C_{\text{trace}}}{C_{\text{ref}}} \sim \frac{3}{2} j\sqrt{\frac{\ell^2}{D\tau}}$. Since Eq. (17) is calculated for $\tau \sim \ell/U_{\text{ref}}$, $\frac{C_{\text{trace}}}{C_{\text{ref}}} \sim \frac{3}{2} j\text{Pe}^{1/2} \ll c_s \sim O[j\log(\frac{1}{\epsilon})]$. Therefore, solute concentration generated due to surface activity is significantly higher than the trace solute concentration, which enables us to employ the quasi-steady state assumption.

III. RESULTS AND DISCUSSION

A. Validation

For a given $j(s)$, q, and θ, Eqs. (4), (15), and (17) can be employed to calculate the particle trajectory. To test the validity of our approach, we compare our predictions with the experimental trajectories of an L-shaped thermophoretic particle, as described in Kümmel *et al.* [85]. We note that the L-shaped particle utilized by the authors does not consist of cylindrical arms. However, at the slender limit, the cross-sectional geometry will have a minor impact on the calculations. Therefore, we are able to use the methodology described above.

The geometry of L-shaped particle in Kümmel *et al.* [85] yields $\ell = 12\ \mu$m, $\epsilon = 0.125$, $q = -\frac{1}{8}$, and $\theta = \frac{\pi}{2}$. Since only the positive arm of the L-shaped geometry in Kümmel *et al.* [85] is active, $j(s) = H(s)$, where H is the Heaviside function. Substituting geometric values and $j(s) = H(s)$ in Eq. (4), we evaluate $\mathbf{U}$ and $\boldsymbol{\Omega}$ by using Eq. (15), and obtain the trajectory through Eq. (17). First, we are able to recover the circular trajectory observed experimentally by Kümmel *et al.* [85]. Further, we obtain $\ell\mathscr{R} = 8.1\ \mu$m, which is in the same order of magnitude as the experimentally reported radius of 7.5 μm. We acknowledge that the comparison between our estimate and the experiments of Kümmel *et al.* [85] is only qualitative since we do not account for localized heating effects [98]. We note while the values of $\mathbf{U}$ and $\boldsymbol{\Omega}$ are dependent on the magnitude of j and ϵ, the value of $\mathscr{R}$ is independent of the magnitude j and ϵ, and is only a function of q and θ. Therefore, in the quantitative estimate described above for the experimental observations of Kümmel *et al.* [85], we only used the values of q, θ, ϵ, and ℓ, and did not require any additional parameters. Physically, this result implies that the radius of the circular trajectory of the particle is less sensitive to the magnitude of the reactive flux and the slenderness of the geometry. However, both the speed of the particle and the frequency of rotation increase with an increase in slenderness, i.e., lower ϵ, and an increase in reactive flux.

Interestingly, for $j(s) = H(s)$, $\Delta c_0^{q+\frac{1}{2}} = 0$ and $\Delta c^0_{q-\frac{1}{2}} \neq 0$, see Figs. 2(a) and 2(b). This finding implies that for $j(s) = H(s)$, the concentration about the active arm is symmetric and the concentration difference across it is negligible. The 3×1 matrix in the right-hand side of Eq. (15) is the effective force and torque generated by the active propulsion mechanism. Since $\Delta c_0^{q+\frac{1}{2}} = 0$ for $j(s) = H(s)$, the effective force and torque are driven solely by the diffusive tail on the negative arm, i.e., the passive arm. Furthermore, our analysis reveals that the effective force is parallel to the passive arm. This result is in contrast to the findings of Kümmel *et al.* [85], who assumed that a force is applied perpendicular to the active arm. In fact, our analysis enables us to move away from the artificial force and torque approach [87], as we are able to evaluate the effective force and torque by utilizing the Lorentz reciprocal theorem. Our analysis suggests that, for multiple arms, the effective force $\mathbf{F}_{\text{eff}} \propto \sum_i \Delta c_0^i \mathbf{e}_{ti}$, where Δc_0^i is the concentration difference along the ith arm and $\mathbf{e}_{ti}$ is the parallel vector to the arm.

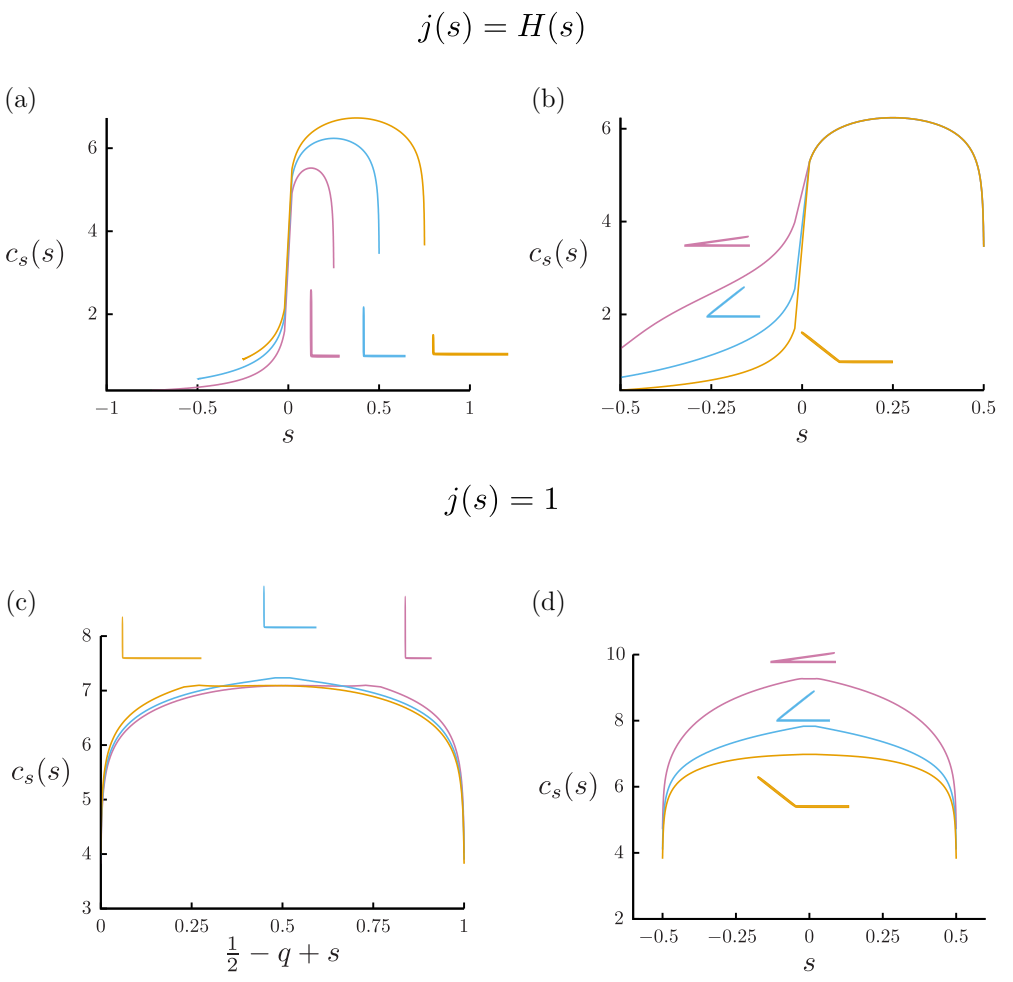

FIG. 2. Surface concentration $c_s(s)$ for different combinations of q, θ and $j(s)$. (a, b) $j(s) = H(s)$ and (c,d) $j(s) = 1$. (a, c) $\theta = \frac{\pi}{2}$ and $q = -0.25$ (pink), $q = 0$ (blue), and $q = 0.25$ (yellow). (b, d) $q = 0$ and $\theta = \frac{\pi}{18}$ (pink), $\theta = \frac{\pi}{4}$ (blue), and $\theta = \frac{3\pi}{4}$ (yellow). $\epsilon = 10^{-3}$ for all cases.

B. Uniform surface flux

To gain deeper insight into the impact of q and θ on the motion of particles, we consider the scenario of $j(s) = 1$. Under this assumption, the particle motion is solely driven by geometrical asymmetry since the entire particle is uniformly active. In Fig. 2(c), when the angle between the arms is fixed to $\theta = \frac{\pi}{2}$, $c_s(s + \frac{1}{2} - q)$ is relatively insensitive to q. Physically, the concentration at the hinge is dominated by the activity on two sides of the bend. Therefore, the concentration near the hinge is relatively insensitive to the location of the hinge. In contrast, the concentration at the end will be determined by the activity along the whole length of the particle. Thus the more distant end will have a lower concentration. In contrast, for equal arm lengths ($q = 0$), a change in θ has significant impact on $c_s(s)$; see Fig. 2(d). This occurs because the relative distance between any point on the particle surface with respect to the other arm changes significantly with θ. For smaller angles, the relative distance between the arms decreases and thus the surface concentration is higher.

By employing Eqs. (4), (15), and (17), we obtain particle trajectories for a combination of different q and θ values; see Fig. 3. We find that when the two arms are of equal lengths, i.e.,

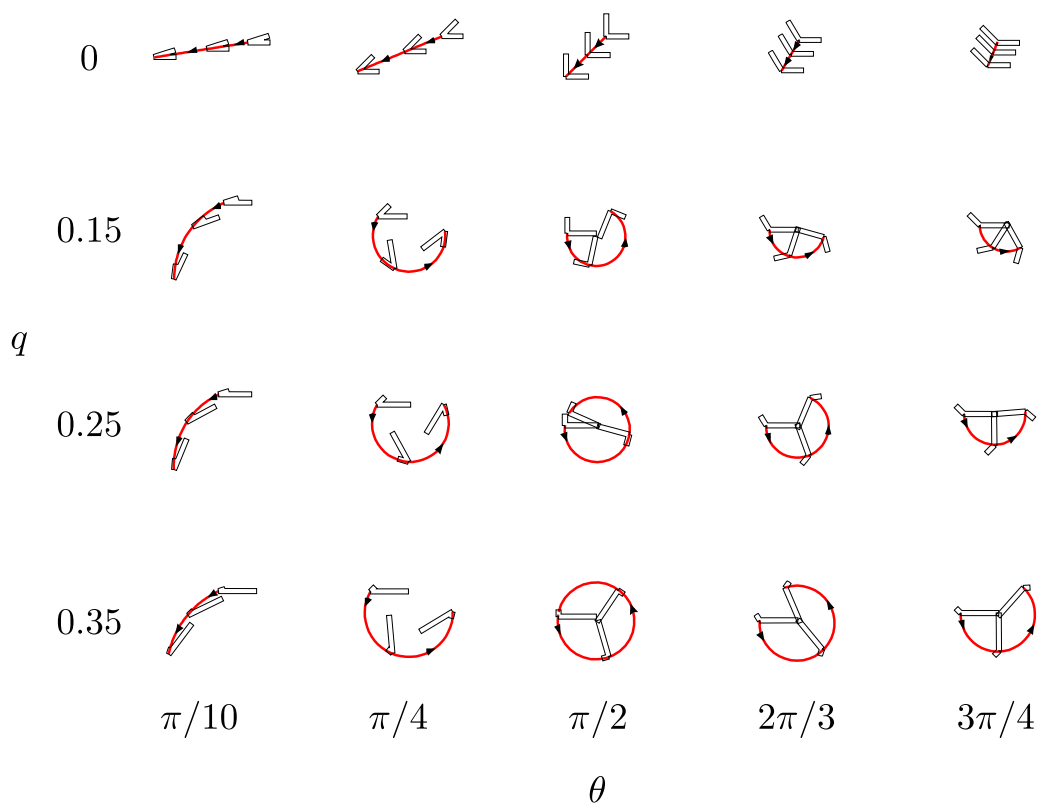

FIG. 3. Particle trajectories for $j(s) = 1$ and for different q and θ. All the trajectories are calculated up to the time period of rotation for the particle with $q = 0.35$ and $\theta = \frac{\pi}{2}$. The trajectories of individual particles are not drawn to a fixed scale; only the total length of each particle is 1. $\epsilon = 10^{-3}$ for all trajectories.

$q = 0$, the particle moves in a straight line ($\Omega_3 = 0$) irrespective of θ. For $q = 0$, due to symmetry, $\Delta c_0^{q+\frac{1}{2}} + \Delta c_{q-\frac{1}{2}}^0 = 0$; see Fig. 2(d). Therefore, the effective torque on the particle $\mathbf{T}_{\text{eff}} \cdot \mathbf{e}_3 = 0$; see Eq. (15). In addition, the rotation-translation coupling terms also cancel out. Mathematically, $\tilde{b}_{13}\mathbf{F}_{\text{eff}} \cdot \mathbf{e}_1 + \tilde{b}_{23}\mathbf{F}_{\text{eff}} \cdot \mathbf{e}_2 = 0$, see Eqs. (15) and (B2). Therefore, for $q = 0$, the net turning induced by geometric asymmetry is zero and the particles only translate. For $q \neq 0$, we also see a second set of characteristic contours where $\Omega_3 = 0$. Here, $\Delta c_0^{q+\frac{1}{2}} + \Delta c_{q-\frac{1}{2}}^0 \neq 0$. However, for specific combinations of q and θ, we still observe that $\tilde{b}_{13}\mathbf{F}_{\text{eff}} \cdot \mathbf{e}_1 + \tilde{b}_{23}\mathbf{F}_{\text{eff}} \cdot \mathbf{e}_2 = 0$ and $\mathbf{T}_{\text{eff}} \cdot \mathbf{e}_3 = 0$ individually. Therefore, the particle only translates. These two contours for $\Omega_3 = 0$ are shown in Fig. 4 with dashed lines. For all other cases, we observe that the particle turns; see Fig. 3. As is evident from the figure, the degree and speed of turning depend on q and θ.

To understand the quantitative dependence of particle trajectory on geometrical parameters, we construct phase plots for $U_{\text{tot}} = \sqrt{U_1^2 + U_2^2}$ and Ω_3; see Fig. 4. First, we observe that U_{tot} is symmetric about $q = 0$, i.e., $U_{\text{tot}}(q, \theta) = U_{\text{tot}}(-q, \theta)$. This result is consistent with the expectation, i.e., for $j(s) = 1$, switching the positive and negative arms should not influence the speed. In contrast, $\Omega_3(q, \theta) = -\Omega_3(-q, \theta)$, which indicates that the direction of turning switches, but the magnitude remains the same. This dependence agrees with expectation, since changing the sign of q changes the initial orientation, which causes the particle to turn in the opposite direction.

One of the key features that emerges from Fig. 4 is the presence of a maximum in U_{tot} and Ω_3 around $\theta \approx \frac{\pi}{2}$ and $q \approx 0.3$. Therefore, the maximum U_{tot} and Ω_3 is observed for an L-shaped

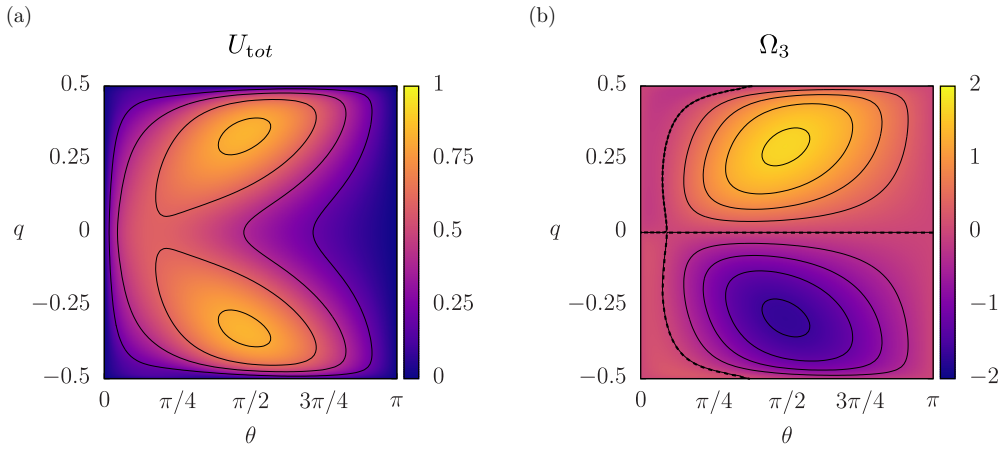

FIG. 4. Phase plots for $j(s) = 1$ and $\epsilon = 10^{-3}$. (a) The speed of the particle $\sqrt{U_1^2 + U_2^2}$. (b) The angular velocity of the particle Ω_3. A maximum in U_{tot} and Ω_3 is observed for $q \approx 0.3$ and $\theta \approx \frac{\pi}{2}$. The $\Omega_3 = 0$ contours are annotated using bold dashed lines. $\epsilon = 10^{-3}$ for both plots.

particle with one arm 4 times as long as the other one. We write Eq. (15) as follows:

$$\begin{bmatrix} \mathbf{U} \\ \mathbf{\Omega} \end{bmatrix} = \mathscr{A}\mathbf{M}(q,\theta) \cdot \begin{bmatrix} \mathbf{F}_{\text{eff}}(q,\theta) \\ \mathbf{T}_{\text{eff}}(q,\theta) \end{bmatrix}, \tag{18}$$

where $\mathbf{M}$ is the hydrodynamic mobility and $\mathbf{F}_{\text{eff}}$ and $\mathbf{T}_{\text{eff}}$ are the effective driving propulsion force and torque. The geometric parameters q and θ influence $\mathbf{M}$, $\mathbf{F}_{\text{eff}}$, and $\mathbf{T}_{\text{eff}}$, but the impact of q and θ is different on $\mathbf{F}_{\text{eff}}$ and $\mathbf{T}_{\text{eff}}$. For instance, $\mathbf{F}_{\text{eff}}$ is dependent on $\Delta c_0^{q+\frac{1}{2}}$ and $\Delta c^0_{q-\frac{1}{2}}$, which are less sensitive to q and more sensitive to θ; see Figs. 2(c) and 2(d). $\mathbf{T}_{\text{eff}}$ has a similar dependence on θ but also varies with q. In contrast, the mobility parameter $\mathbf{M}$ is more sensitive to q than θ; see Appendix B. The interplay of mobility and driving force yields the optimum values of q and θ. We note that these optimal values will change if a different $j(s)$ is used, since that will directly impact the values of $\mathbf{F}_{\text{eff}}$, and $\mathbf{T}_{\text{eff}}$.

We note that the dependence of ϵ in Eq. (18) only comes from $\mathscr{A}$. This occurs because we ignore the higher order corrections in $\mathbf{M}$, $\mathbf{F}_{\text{eff}}$, and $\mathbf{T}_{\text{eff}}$. To this end, we acknowledge that our analysis will be less applicable when the interactions between the two rods are significant. Additionally, our analysis does not focus on circumferential variation of chemical activity, which could be important in certain scenarios, as discussed in Refs. [83,84,86]. Even with these limitations, our analysis provides a convenient starting point to predict trajectories and design self-propelling composite slender bodies.

IV. CONCLUDING REMARKS

In summary, this article presents a theoretical analysis to predict the two-dimensional motion of self-propelling bent rods. By employing slender body theory and the Lorentz reciprocal theorem, we derive Eqs. (4), (15), and (17) to predict the particle trajectories for given q, θ, and $j(s)$. Our analysis reveals that the trajectory of the particle is circular, such that the radius is dependent on q and θ, and is insensitive to the slenderness parameter ϵ. The speed and the frequency of the particle are dependent on the values of q, θ, and ϵ, and display an optimum with the phase plot of q and θ. The results outlined here provide a convenient method to design self-propellers for microbot applications in diagnostics and drug delivery [7,8]. For instance, if the propeller is required to travel in a straight line, then the propeller should have symmetric arms. If the propeller is required to move

and turn faster, then optimum values of q and θ and a smaller ϵ should be utilized. Physically, our analysis also helps to clarify the role of the particle geometry in hydrodynamic mobility as well as the self-propelling driving force. As such, we can move away from the external force and torque approach, and show that the self-propulsion is driven by the concentration differences across each arm. In the future, our work can be extended to more complex geometries, such as slender bodies with multiple arms and activity profiles with circumferential variation.

ACKNOWLEDGMENTS

The authors acknowledge R. Davis, B. Rallabandi, J. Roggeveen, and H. Stone for their helpful input in the preparation of this manuscript. We also thank F. Henrique, N. Jarvey, R. Raj, and G. Roure for their helpful discussions and feedback leading to the culmination of this work. Acknowledgment is made to the Donors of the American Chemical Society Petroleum Research Fund for support of this research.

APPENDIX A: DERIVATION OF SURFACE CONCENTRATION

Ignoring any circumferential dependence, we rewrite Eqs. (2) and (3a) in cylindrical coordinates as

$$\frac{1}{r}\frac{\partial}{\partial r}\left(r\frac{\partial c}{\partial r}\right)+\frac{\partial^2 c}{\partial s^2}=0,\ r>\epsilon, \tag{A1a}$$

$$\epsilon\frac{\partial c}{\partial r}=-j(s),\ r=\epsilon, \tag{A1b}$$

and $c(r\to\infty)\to 0$. To solve our system of equations and obtain the surface concentration $c_s(s)$, we divide the fluid volume into an inner region and an outer region in the radial direction $\mathbf{e}_r$. In the inner region, we introduce a stretched radial coordinate $\rho = r/\epsilon$. The concentration in the inner region is denoted by c^i. Equations (A1a) and (A1b) in the inner region can be written as

$$\frac{1}{\rho}\frac{\partial}{\partial \rho}\left(\rho\frac{\partial c^i}{\partial \rho}\right)+\epsilon^2\frac{\partial^2 c^i}{\partial s^2}=0,\ \rho>1, \tag{A2a}$$

$$\frac{\partial c^i}{\partial \rho}=-j(s),\ \rho=1. \tag{A2b}$$

We expand the solute concentration in the inner region in orders of ϵ; $c^i = c^i_0 + \epsilon c^i_1 + O(\epsilon^2)$ and solve for the leading order and first order solutions. The resultant concentration profile in the inner region is found to be

$$c^i = -j(s)\log\rho + K(z;\epsilon) + O(\epsilon^2), \tag{A3}$$

where K in Eq. (A3) is obtained by matching with the outer solution.

In the outer region, we represent the concentration c^o as being due to a distribution of sources $\alpha(s)$ along an infinitesimally thin space curve along the particle centerline. The position of any point in the fluid volume $\mathbf{x}(r, s) = s\mathbf{e}_t(s) + r\mathbf{e}_r(s)$. The outer region concentration is represented as

$$c^o = \int_{q-\frac{1}{2}}^{q+\frac{1}{2}} \frac{\alpha(s')}{|\mathbf{x}(r,s)-s'\mathbf{e}_t(s')|}\,ds'. \tag{A4}$$

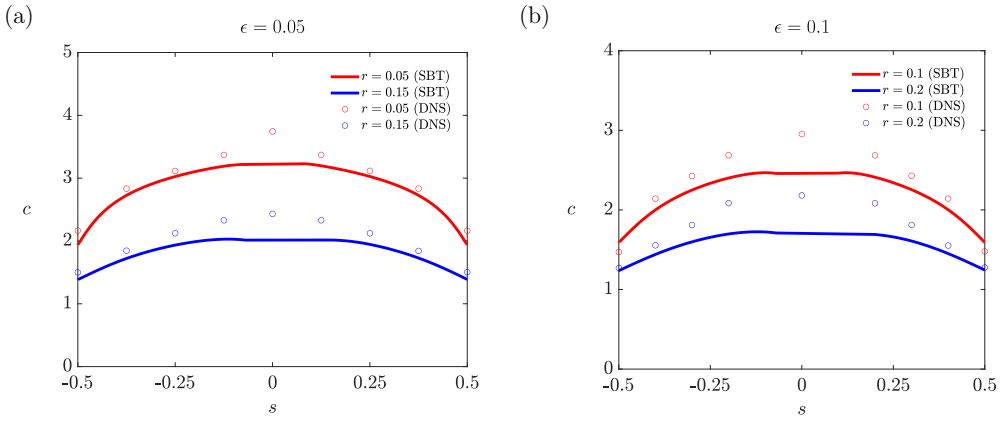

FIG. 5. Comparison of concentration profiles of slender body theory with direct numerical simulations for $j(s) = 1$, $q = 0$, and $\theta = \frac{\pi}{2}$. (a) For $\epsilon = 0.05$. (b) For $\epsilon = 0.1$.

Note that the concentration field in the outer region, proposed in Eq. (A4), decays to zero in the far-field. By using Eq. (1), we evaluate the concentration profile to be

$$c^o = \begin{cases} \displaystyle\int_{q-\frac{1}{2}}^{0} \frac{\alpha(s')}{[(s-s')^2+r^2]^{1/2}}\, ds' + \int_{0}^{q+\frac{1}{2}} \frac{\alpha(s')}{[(s+s'\cos\theta)^2+(r+s'\sin\theta)^2]^{1/2}}\, ds' & s < 0, \\ \displaystyle\int_{q-\frac{1}{2}}^{0} \frac{\alpha(s')}{[(s+s'\cos\theta)^2+(r+s'\sin\theta)^2]^{1/2}}\, ds' + \int_{0}^{q+\frac{1}{2}} \frac{\alpha(s')}{[(s-s')^2+r^2]^{1/2}}\, ds' & s \geqslant 0. \end{cases} \tag{A5}$$

Due to the singularity in Eq. (A5), we propose a substitution of variables $\zeta = s' - s$ and integrate. For $s \geqslant 0$

$$c^o(r, s \geqslant 0) = \alpha(s) \int_{-s}^{q+\frac{1}{2}-s} \frac{d\zeta}{[\zeta^2+r^2]^{1/2}} + \int_{-s}^{q+\frac{1}{2}-s} \frac{\alpha(s+\zeta)-\alpha(s)}{[\zeta^2+r^2]^{1/2}}\, d\zeta + \int_{q-\frac{1}{2}-s}^{-s} \frac{\alpha(s+\zeta)}{\left[(s+\zeta)^2+2(s\cos\theta+r\sin\theta)(s+\zeta)+s^2+r^2\right]^{1/2}}\, d\zeta. \tag{A6}$$

Similarly, we can separate out the singularity for $s < 0$. The integrals demonstrate that $c^o(r, s) = -2\alpha(s)\log r + c_1^o + O(\epsilon)$. To match the outer solution to the inner solution from Eq. (A3), we write $\lim_{\rho\to\infty} c^i = \lim_{r\to 0} c^o$, which shows $\alpha(s) = \frac{j(s)}{2}$. The surface concentration thus at the slip plane is written as Eq. (4). To evaluate the integrals in Eq. (4), one needs to remove the singularity, as shown in Eq. (A6).

To validate our analysis and explore the limits of first-order slender body theory we compare our results to direct numerical simulations (DNS). We compare the concentration of solute around a uniformly reactive ($j(s) = 1$) and symmetric bent-rod ($q = 0$, $\theta = \frac{\pi}{2}$) at different radial distances, see Fig. 5. The direct numerical simulations are performed in COMSOL. The bent-rod geometry is created with a circular cross-section and equal arm lengths. The cross-sectional radii were $r = 0.05$ [Fig. 5(a)] and $r = 0.1$ [Fig. 5(b)], while the axial length is $\ell = 1$. The hinge is beveled to enable a standard numerical solver to resolve the hinge. A constant surface reaction is defined on the particle surface. In the far field, the concentration is matched with a concentration profile of an equivalent point source. The equivalent point source boundary condition reduces numerical errors when compared to a vanishing concentration boundary condition due to finite size of the domain. The concentration was evaluated at the circumferential angle corresponding to the points on the upper outline of the rod in Fig. 1. The concentration profiles in Fig. 5 display a reasonable

TABLE I. For $q = 0$, SBT analysis suggests $\Delta c_0^{q+\frac{1}{2}} + \Delta c^0_{q-\frac{1}{2}} = 0$. We numerically test this through DNS for different θ values. $\epsilon = 0.1$ and $q = 0$ for all scenarios.

θ	DNS	SBT
$\pi/18$	0.008	0
$\pi/6$	0.005	0
$\pi/4$	0.01	0
$\pi/3$	0.007	0
$\pi/2$	0.006	0
$2\pi/3$	0.008	0

quantitative agreement between direct numerical simulations and slender body theory, even for $\epsilon = 0.05$. We note that the agreement becomes worse for $\epsilon = 0.1$, as expected.

To probe the validity of our calculations at different values of θ, we verify if direct numerical simulations adhere to $\Delta c_0^{q+\frac{1}{2}} + \Delta c^0_{q-\frac{1}{2}} = 0$ for $q = 0$. Consequently, we measured the concentration at the hinge and the two ends. In Table I, we report the values of $\Delta c_0^{q+\frac{1}{2}} + \Delta c^0_{q-\frac{1}{2}}$. We find very good quantitative agreement between SBT and DNS. Therefore, we assert that our calculations are able to capture the key effects from an active slender bent-rod geometry. For a more in-depth and rigorous comparison between slender body theory and numerical solutions, we refer the readers to Ref. [82].

We note that the concentration profiles provided in Fig. 2 display a discontinuity in gradients at the hinge. This is expected since the first-order slender body theory ignores higher-order corrections. These corrections become important when the distance between two locations on the rod is $O\left(\frac{1}{\log(\frac{1}{\epsilon})}\right)$. These corrections can, for instance, introduce circumferential variations in the concentration, especially for small θ values [82].

APPENDIX B: DETERMINING THE MOBILITY COEFFICIENTS FOR A SLENDER BENT ROD

The resistance coefficients described Eq. (13) are given as (see Roggeveen and Stone [88])

$$\begin{bmatrix} A_{11} \\ A_{12} \\ A_{22} \\ \tilde{B}_{13} \\ \tilde{B}_{23} \\ C_{33} \end{bmatrix} = -\begin{bmatrix} \frac{1}{8}[5 - 2q + (2q-1)\cos 2\theta] \\ \frac{1}{8}(2q-1)\sin 2\theta \\ 1 + \frac{1}{4}(2q-1)\sin^2\theta \\ -\frac{1}{8}(1-2q)^2\sin\theta \\ \frac{1}{8}\left[(2q+1)^2 + (1-2q)^2\cos\theta\right] \\ \frac{1}{12} + q^2 \end{bmatrix}. \tag{B1}$$

We invert $\mathbf{R}$ and obtain the following mobility coefficients

$$\begin{bmatrix} a_{11} \\ a_{12} \\ a_{22} \\ \tilde{b}_{13} \\ \tilde{b}_{23} \\ c_{33} \end{bmatrix} = -\frac{1}{\mathscr{L}}\begin{bmatrix} -\frac{1}{64}[(1+2q)^2 + (1-2q)^2\cos\theta]^2 + (\frac{1}{12} + q^2)[1 + \frac{1}{4}(-1+2q)\sin^2\theta] \\ -\frac{1}{64}(1-2q)^2[(1+2q)^2 + (1-2q)^2\cos\theta]\sin\theta - \frac{1}{8}(-1+2q)(\frac{1}{12} + q^2)\sin 2\theta \\ \frac{1}{8}(\frac{1}{12} + q^2)[5 - 2q + (-1+2q)\cos 2\theta] - \frac{1}{64}(1-2q)^4\sin^2\theta \\ \frac{1}{32}(-1+2q)[-3 + 4q + 4q^2 + (1+2q)^2\cos\theta]\sin\theta \\ \frac{1}{64}(-\{[(1+2q)^2 + (1-2q)^2\cos\theta][5 - 2q + (-1+2q)\cos 2\theta]\} - 2(-1+2q)^3\cos\theta\sin^2\theta) \\ \frac{1}{32}[17 - 4q^2 + (-1+4q^2)\cos 2\theta] \end{bmatrix}, \tag{B2}$$

where $\mathscr{L} = \frac{1}{768}[19 + 88q^2 - 144q^4 - 12(1-4q^2)^2\cos\theta + (1 + 8q^2 - 48q^4)\cos 2\theta]$.

[1] J. Elgeti, R. G. Winkler, and G. Gompper, Physics of microswimmers—Single-particle motion and collective behavior: A review, Rep. Prog. Phys. **78**, 056601 (2015).
[2] E. M. Purcell, Life at low Reynolds number, Am. J. Phys. **45**, 3 (1977).
[3] H. C. Berg and L. Turner, Chemotaxis of bacteria in glass capillary arrays: *Escherichia coli*, motility, microchannel plate, and light scattering, Biophys. J. **58**, 919 (1990).
[4] E. Lauga and T. R. Powers, The hydrodynamics of swimming microorganisms, Rep. Prog. Phys. **72**, 096601 (2009).
[5] E. Lauga, W. R. DiLuzio, G. M. Whitesides, and H. A. Stone, Swimming in circles: Motion of bacteria near solid boundaries, Biophys. J. **90**, 400 (2006).
[6] E. Lauga, Bacterial hydrodynamics, Annu. Rev. Fluid Mech. **48**, 105 (2016).
[7] B. J. Nelson, I. K. Kaliakatsos, and J. J. Abbott, Microrobots for minimally invasive medicine, Annu. Rev. Biomed. Eng. **12**, 55 (2010).
[8] A.-I. Bunea and R. Taboryski, Recent advances in microswimmers for biomedical applications, Micromachines **11**, 1048 (2020).
[9] S. Sundararajan, P. E. Lammert, A. W. Zudans, V. H. Crespi, and A. Sen, Catalytic motors for transport of colloidal cargo, Nano Lett. **8**, 1271 (2008).
[10] J. Burdick, R. Laocharoensuk, P. M. Wheat, J. D. Posner, and J. Wang, Synthetic nanomotors in microchannel networks: Directional microchip motion and controlled manipulation of cargo, J. Am. Chem. Soc. **130**, 8164 (2008).
[11] C. Maggi, J. Simmchen, F. Saglimbeni, J. Katuri, M. Dipalo, F. De Angelis, S. Sanchez, and R. Di Leonardo, Self-assembly of micromachining systems powered by Janus micromotors, Small **12**, 446 (2016).
[12] P. Sharan, A. Nsamela, S. C. Lesher-Pérez, and J. Simmchen, Microfluidics for microswimmers: Engineering novel swimmers and constructing swimming lanes on the microscale: A tutorial review, Small **17**, 2007403 (2021).
[13] T. Sanchez, D. T. Chen, S. J. DeCamp, M. Heymann, and Z. Dogic, Spontaneous motion in hierarchically assembled active matter, Nature (London) **491**, 431 (2012).
[14] M. Guix, J. Orozco, M. Garcia, W. Gao, S. Sattayasamitsathit, A. Merkoçi, A. Escarpa, and J. Wang, Superhydrophobic alkanethiol-coated microsubmarines for effective removal of oil, ACS Nano **6**, 4445 (2012).
[15] J. Li, O. E. Shklyaev, T. Li, W. Liu, H. Shum, I. Rozen, A. C. Balazs, and J. Wang, Self-propelled nanomotors autonomously seek and repair cracks, Nano Lett. **15**, 7077 (2015).
[16] I.-A. Pavel, G. Salinas, M. Mierzwa, S. Arnaboldi, P. Garrigue, and A. Kuhn, Cooperative chemotaxis of magnesium microswimmers for corrosion spotting, ChemPhysChem **22**, 1321 (2021).
[17] A. Ghosh and P. Fischer, Controlled propulsion of artificial magnetic nanostructured propellers, Nano Lett. **9**, 2243 (2009).
[18] J. Lim, C. Lanni, E. R. Evarts, F. Lanni, R. D. Tilton, and S. A. Majetich, Magnetophoresis of nanoparticles, ACS Nano **5**, 217 (2011).
[19] F. Alnaimat, S. Dagher, B. Mathew, A. Hilal-Alnqbi, and S. Khashan, Microfluidics based magnetophoresis: A review, Chem. Rec. **18**, 1596 (2018).
[20] G. A. Roure and F. R. Cunha, On the magnetization of a dilute suspension in a uniform magnetic field: Influence of dipolar and hydrodynamic particle interactions, J. Magn. Magn. Mater. **513**, 167082 (2020).
[21] N. Bertin, T. A. Spelman, O. Stephan, L. Gredy, M. Bouriau, E. Lauga, and P. Marmottant, Propulsion of Bubble-Based Acoustic Microswimmers, Phys. Rev. Appl. **4**, 064012 (2015).
[22] F. Nadal and S. Michelin, Acoustic propulsion of a small, bottom-heavy sphere, J. Fluid Mech. **898**, A10 (2020).
[23] F. Nadal and E. Lauga, Asymmetric steady streaming as a mechanism for acoustic propulsion of rigid bodies, Phys. Fluids **26**, 082001 (2014).
[24] T. Xu, L.-P. Xu, and X. Zhang, Ultrasound propulsion of micro-/nanomotors, Appl. Mater. Today **9**, 493 (2017).
[25] J. McNeill, N. Sinai, J. Wang, V. Oliver, E. Lauga, F. Nadal, and T. E. Mallouk, Purely viscous acoustic propulsion of bimetallic rods, Phys. Rev. Fluids **6**, L092201 (2021).

[26] J. Voß and R. Wittkowski, Propulsion of bullet- and cup-shaped nano- and microparticles by traveling ultrasound waves, Phys. Fluids **34**, 052007 (2022).
[27] L. Ren, W. Wang, and T. E. Mallouk, Two forces are better than one: Combining chemical and acoustic propulsion for enhanced micromotor functionality, Acc. Chem. Res. **51**, 1948 (2018).
[28] J. Voß and R. Wittkowski, Orientation-dependent propulsion of triangular nano-and microparticles by a traveling ultrasound wave, ACS Nano **16**, 3604 (2022).
[29] S. Mohanty, I. S. Khalil, and S. Misra, Contactless acoustic micro/nano manipulation: A paradigm for next generation applications in life sciences, Proc. R. Soc. A **476**, 20200621 (2020).
[30] A. S. Khair and J. K. Kabarowski, Migration of an electrophoretic particle in a weakly inertial or viscoelastic shear flow, Phys. Rev. Fluids **5**, 033702 (2020).
[31] A. Yee and M. Yoda, Experimental observations of bands of suspended colloidal particles subject to shear flow and steady electric field, Microfluid. Nanofluid. **22**, 113 (2018).
[32] A. S. Khair, Nonlinear electrophoresis of colloidal particles, Curr. Opin. Colloid Interface Sci. **59**101587 (2022).
[33] E. Saad and M. Faltas, Time-dependent electrophoresis of a dielectric spherical particle embedded in Brinkman medium, Z. Angew. Math. Phys. **69**, 43 (2018).
[34] A. M. Brooks, M. Tasinkevych, S. Sabrina, D. Velegol, A. Sen, and K. J. M. Bishop, Shape-directed rotation of homogeneous micromotors via catalytic self-electrophoresis, Nat. Commun. **10**, 495 (2019).
[35] A. S. Khair, Strong deformation of the thick electric double layer around a charged particle during sedimentation or electrophoresis, Langmuir **34**, 876 (2018).
[36] S. Gangwal, O. J. Cayre, M. Z. Bazant, and O. D. Velev, Induced-Charge Electrophoresis of Metallodielectric Particles, Phys. Rev. Lett. **100**, 058302 (2008).
[37] T. M. Squires and M. Z. Bazant, Induced-charge electro-osmosis, J. Fluid Mech. **509**, 217 (2004).
[38] T. M. Squires and M. Z. Bazant, Breaking symmetries in induced-charge electro-osmosis and electrophoresis, J. Fluid Mech. **560**, 65 (2006).
[39] M. Z. Bazant and T. M. Squires, Induced-charge electrokinetic phenomena, Curr. Opin. Colloid Interface Sci. **15**, 203 (2010).
[40] A. S. Khair and B. Balu, Breaking electrolyte symmetry in induced-charge electro-osmosis, J. Fluid Mech. **905**, A20 (2020).
[41] A. M. Brooks, S. Sabrina, and K. J. M. Bishop, Shape-directed dynamics of active colloids powered by induced-charge electrophoresis, Proc. Natl. Acad. Sci. USA **115**, E1090 (2018).
[42] J. G. Lee, A. M. Brooks, W. A. Shelton, K. J. M. Bishop, and B. Bharti, Directed propulsion of spherical particles along three dimensional helical trajectories, Nat. Commun. **10**, 2575 (2019).
[43] S. Oren and I. Frankel, Induced-charge electrophoresis of ideally polarizable particle pairs, Phys. Rev. Fluids **5**, 094201 (2020).
[44] D. Velegol, A. Garg, R. Guha, A. Kar, and M. Kumar, Origins of concentration gradients for diffusiophoresis, Soft Matter **12**, 4686 (2016).
[45] B. Abécassis, C. Cottin-Bizonne, C. Ybert, A. Ajdari, and L. Bocquet, Boosting migration of large particles by solute contrasts, Nat. Mater. **7**, 785 (2008).
[46] A. Banerjee, I. Williams, R. N. Azevedo, M. E. Helgeson, and T. M. Squires, Soluto-inertial phenomena: Designing long-range, long-lasting, surface-specific interactions in suspensions, Proc. Natl. Acad. Sci. USA **113**, 8612 (2016).
[47] A. Gupta, B. Rallabandi, and H. A. Stone, Diffusiophoretic and diffusioosmotic velocities for mixtures of valence-asymmetric electrolytes, Phys. Rev. Fluids **4**, 043702 (2019).
[48] A. Gupta, S. Shim, and H. A. Stone, Diffusiophoresis: From dilute to concentrated electrolytes, Soft Matter **16**, 6975 (2020).
[49] B. M. Alessio, S. Shim, E. Mintah, A. Gupta, and H. A. Stone, Diffusiophoresis and diffusioosmosis in tandem: Two-dimensional particle motion in the presence of multiple electrolytes, Phys. Rev. Fluids **6**, 054201 (2021).
[50] R. Piazza, Thermophoresis: moving particles with thermal gradients, Soft Matter **4**, 1740 (2008).
[51] X. Lin, T. Si, Z. Wu, and Q. He, Self-thermophoretic motion of controlled assembled micro-/nanomotors, Phys. Chem. Chem. Phys. **19**, 23606 (2017).

[52] M. Yang and M. Ripoll, Simulations of thermophoretic nanoswimmers, Phys. Rev. E **84**, 061401 (2011).
[53] P. Gaspard and R. Kapral, The stochastic motion of self-thermophoretic Janus particles, J. Stat. Mech. (2019) 074001.
[54] Y. L. Chen, C. X. Yang, and H. R. Jiang, Electrically enhanced self-thermophoresis of laser-heated Janus particles under a rotating electric field, Sci. Rep. **8**, 5945 (2018).
[55] W. Qin, T. Peng, Y. Gao, F. Wang, X. Hu, K. Wang, J. Shi, D. Li, J. Ren, and C. Fan, Catalysis-driven self-thermophoresis of Janus plasmonic nanomotors, Angew. Chem. **129**, 530 (2017).
[56] H. R. Jiang, N. Yoshinaga, and M. Sano, Active Motion of a Janus Particle by Self-Thermophoresis in a Defocused Laser Beam, Phys. Rev. Lett. **105**, 268302 (2010).
[57] W. F. Paxton, K. C. Kistler, C. C. Olmeda, A. Sen, S. K. St. Angelo, Y. Cao, T. E. Mallouk, P. E. Lammert, and V. H. Crespi, Catalytic nanomotors: Autonomous movement of striped nanorods, J. Am. Chem. Soc. **126**, 13424 (2004).
[58] M. N. Popescu, W. E. Uspal, and S. Dietrich, Self-diffusiophoresis of chemically active colloids, Eur. Phys. J. Spec. Top. **225**, 2189 (2016).
[59] P. M. Wheat, N. A. Marine, J. L. Moran, and J. D. Posner, Rapid fabrication of bimetallic spherical motors, Langmuir **26**, 13052 (2010).
[60] A. M. Davis and E. Yariv, Self-diffusiophoresis of Janus particles at large Damköhler numbers, J. Eng. Math. **133**, 5 (2022).
[61] C. H. Meredith, A. C. Castonguay, Y. J. Chiu, A. M. Brooks, P. G. Moerman, P. Torab, P. K. Wong, A. Sen, D. Velegol, and L. D. Zarzar, Chemical design of self-propelled Janus droplets, Matter **5**, 616 (2022).
[62] C. H. Meredith, P. G. Moerman, J. Groenewold, Y. J. Chiu, W. K. Kegel, A. van Blaaderen, and L. D. Zarzar, Predator–prey interactions between droplets driven by nonreciprocal oil exchange, Nat. Chem. **12**, 1136 (2020).
[63] E. Kanso and S. Michelin, Phoretic and hydrodynamic interactions of weakly confined autophoretic particles, J. Chem. Phys. **150**, 044902 (2019).
[64] T. Speck, Thermodynamic approach to the self-diffusiophoresis of colloidal Janus particles, Phys. Rev. E **99**, 060602(R) (2019).
[65] P. Chatterjee, E. M. Tang, P. Karande, and P. T. Underhill, Propulsion of catalytic Janus spheres in viscosified newtonian solutions, Phys. Rev. Fluids **3**, 014101 (2018).
[66] M. N. Popescu, W. E. Uspal, C. Bechinger, and P. Fischer, Chemotaxis of active Janus nanoparticles, Nano Lett. **18**, 5345 (2018).
[67] C. Zhou, H. Zhang, J. Tang, and W. Wang, Photochemically powered AgCl Janus micromotors as a model system to understand ionic self-diffusiophoresis, Langmuir **34**, 3289 (2018).
[68] B. Nasouri and R. Golestanian, Exact axisymmetric interaction of phoretically active Janus particles, J. Fluid Mech. **905**, A13 (2020).
[69] R. Pöhnl, M. N. Popescu, and W. E. Uspal, Axisymmetric spheroidal squirmers and self-diffusiophoretic particles, J. Phys.: Condens. Matter **32**, 164001 (2020).
[70] S. J. Ebbens and J. R. Howse, Direct observation of the direction of motion for spherical catalytic swimmers, Langmuir **27**, 12293 (2011).
[71] O. Shemi and M. J. Solomon, Self-propulsion and active motion of Janus ellipsoids, J. Phys. Chem. B **122**, 10247 (2018).
[72] J. P. Hsu, X. C. Luu, and W. L. Hsu, Diffusiophoresis of an ellipsoid along the axis of a cylindrical pore, J. Phys. Chem. B **114**, 8043 (2010).
[73] M. Lisicki, S. Y. Reigh, and E. Lauga, Autophoretic motion in three dimensions, Soft Matter **14**, 3304 (2018).
[74] W. Wang, W. Duan, A. Sen, and T. E. Mallouk, Catalytically powered dynamic assembly of rod-shaped nanomotors and passive tracer particles, Proc. Natl. Acad. Sci. USA **110**, 17744 (2013).
[75] O. Schnitzer and E. Yariv, Osmotic self-propulsion of slender particles, Phys. Fluids **27**, 031701 (2015).
[76] S. Shklyaev, J. F. Brady, and U. M. Córdova-Figueroa, Nonspherical osmotic motor: Chemical sailing, J. Fluid Mech. **748**, 488 (2014).
[77] A. Daddi-Moussa-Ider, B. Nasouri, A. Vilfan, and R. Golestanian, Optimal swimmers can be pullers, pushers or neutral depending on the shape, J. Fluid Mech. **922**, R5 (2021).

[78] G. Hancock, The self-propulsion of microscopic organisms through liquids, Proc. R. Soc. London, Ser. A **217**, 96 (1953).
[79] R. Cox, The motion of long slender bodies in a viscous fluid Part 1. General theory, J. Fluid Mech. **44**, 791 (1970).
[80] G. Batchelor, Slender-body theory for particles of arbitrary cross-section in Stokes flow, J. Fluid Mech. **44**, 419 (1970).
[81] E. Yariv, Self-diffusiophoresis of slender catalytic colloids, Langmuir **36**, 6903 (2019).
[82] R. Poehnl and W. Uspal, Phoretic self-propulsion of helical active particles, J. Fluid Mech. **927**, A46 (2021).
[83] P. Katsamba, S. Michelin, and T. D. Montenegro-Johnson, Slender phoretic theory of chemically active filaments, J. Fluid Mech. **898**, A24 (2020).
[84] P. Katsamba, M. D. Butler, L. Koens, and T. D. Montenegro-Johnson, Chemically active filaments: Analysis and extensions of slender phoretic theory, Soft Matter **18**, 7051 (2022).
[85] F. Kümmel, B. ten Hagen, R. Wittkowski, I. Buttinoni, R. Eichhorn, G. Volpe, H. Löwen, and C. Bechinger, Circular Motion of Asymmetric Self-Propelling Particles, Phys. Rev. Lett. **110**, 198302 (2013).
[86] D. V. Rao, N. Reddy, J. Fransaer, and C. Clasen, Self-propulsion of bent bimetallic Janus rods, J. Phys. D: Appl. Phys. **52**, 014002 (2019).
[87] B. ten Hagen, R. Wittkowski, D. Takagi, F. Kümmel, C. Bechinger, and H. Löwen, Can the self-propulsion of anisotropic microswimmers be described by using forces and torques? J. Phys.: Condens. Matter **27**, 194110 (2015).
[88] J. V. Roggeveen and H. A. Stone, Motion of asymmetric bodies in two-dimensional shear flow, J. Fluid Mech. **939**, A23 (2022).
[89] H. Masoud and H. A. Stone, The reciprocal theorem in fluid dynamics and transport phenomena, J. Fluid Mech. **879**, P1 (2019).
[90] S. Kim and S. J. Karrila, *Microhydrodynamics: Principles and Selected Applications* (Courier Corporation, Boston, MA, 2013).
[91] A. R. Morgan, A. B. Dawson, H. S. Mckenzie, T. S. Skelhon, R. Beanland, H. P. Franks, and S. A. Bon, Chemotaxis of catalytic silica–manganese oxide "matchstick" particles, Mater. Horiz. **1**, 65 (2014).
[92] J. L. Anderson, Colloid transport by interfacial forces, Annu. Rev. Fluid Mech. **21**, 61 (1989).
[93] R. Golestanian, T. Liverpool, and A. Ajdari, Designing phoretic micro- and nano-swimmers, New J. Phys. **9**, 126 (2007).
[94] R. Golestanian, T. B. Liverpool, and A. Ajdari, Propulsion of a Molecular Machine by Asymmetric Distribution of Reaction Products, Phys. Rev. Lett. **94**, 220801 (2005).
[95] C. M. Bender, S. Orszag, and S. A. Orszag, *Advanced Mathematical Methods for Scientists and Engineers I: Asymptotic Methods and Perturbation Theory*, Vol. 1 (Springer Science & Business Media, Berlin, 1999).
[96] K. K. Dey, S. Bhandari, D. Bandyopadhyay, S. Basu, and A. Chattopadhyay, The pH taxis of an intelligent catalytic microbot, Small **9**, 1916 (2013).
[97] J. Anderson, M. Lowell, and D. Prieve, Motion of a particle generated by chemical gradients Part 1. Nonelectrolytes, J. Fluid Mech. **117**, 107 (1982).
[98] S. Samin and R. van Roij, Self-Propulsion Mechanism of Active Janus Particles in Near-Critical Binary Mixtures, Phys. Rev. Lett. **115**, 188305 (2015).